Journal of CO2 Utilization 77 (2023) 102606

Contents lists available at ScienceDirect

Journal of CO2 Utilization

journal homepage: www.elsevier.com/locate/jcou

Experimental optimization of Ni/P atomic ratio for nickel phosphide catalysts in reverse water-gas shift

Gul Hameed [a], Ali Goksu [a], Loukia-Pantzechroula Merkouri [a], Anna Penkova [b], Tomas Ramirez Reina [a,b], Sergio Carrasco Ruiz [b], Melis Seher Duyar [a,*]

[a] *School of Chemistry and Chemical Engineering, University of Surrey, Guildford GU2 7XH, UK*
[b] *Department of Inorganic Chemistry and Materials Sciences Institute, University of Seville-CSIC, 41092 Seville, Spain*

ARTICLE INFO

Keywords:
Reverse water-gas shift
CO_2 utilization
Nickel phosphide
Hydrogenation
Thermochemical CO_2 reduction

ABSTRACT

Nickel phosphide catalysts show a high level of selectivity for the reverse water-gas shift (RWGS) reaction, inhibiting the competing methanation reaction. This work investigates the extent to which suppression of methanation can be controlled by phosphidation and tests the stability of phosphide phases over 24-hour time on stream. Herein the synthesis of different phosphide crystal structures by varying Ni/P atomic ratios (from 0.5 to 2.4) is shown to affect the selectivity to CO over CH_4 in a significant way. We also show that the activity of these catalysts can be fine-tuned by the synthesis Ni/P ratio and identify suitable catalysts for low temperature RWGS process. $Ni_{12}P_5$-SiO_2 showed 80–100% selectivity over the full temperature range (i.e., 300–800 °C) tested, reaching 73% CO_2 conversion at 800 °C. Ni_2P-SiO_2 exhibited CO selectivity of 93–100% over a full temperature range, and 70% CO_2 conversion at 800 °C. The highest CO_2 conversions for $Ni_{12}P_5$-SiO_2 at all temperatures among all catalysts showed its promising nature for CO_2 capture and utilisation. The methanation reaction was suppressed in addition to RWGS activity improvement through the formation of nickel phosphide phases, and the crystal structure was found to determine CO selectivity, with the following order $Ni_{12}P_5 > Ni_2P > Ni_3P$. Based on the activity of the studied catalysts, the catalysts were ranked in order of suitability for the RWGS reaction as follows: $Ni_{12}P_5$-SiO_2 (Ni/P = 2.4) > Ni_2P-SiO_2 (Ni/P = 2) > NiP-SiO_2 (Ni/P = 1) > NiP_2-SiO_2 (Ni/P = 0.5). Two catalysts with Ni/P atomic ratios; 2.4 and 2, were selected for stability testing. The catalyst with Ni/P ratio = 2.4 (i.e., $Ni_{12}P_5$-SiO_2) was found to be more stable in terms of CO_2 conversion and CO yield over the 24-hour duration at 550 °C. Using the phosphidation strategy to tune both selectivity and activity of Ni catalysts for RWGS, methanation as a competing reaction is shown to be no longer a critical issue in the RWGS process for catalysts with high Ni/P atomic ratios (2.4 and 2) even at lower temperatures (300–500 °C). This opens up potential low temperature RWGS opportunities, especially coupled to downstream or tandem lower temperature processes to produce liquid fuels.

1. Introduction

Increasing level of CO_2 in the atmosphere is one of the biggest environmental concerns of our day due to its effects on climate change and sea level, frequent occurrence of forest fires, and the increase in the number of stormy days per year [1,2]. While CO_2 emissions from energy generation (fossil fuel combustion) can be decreased using renewables, carbon is still needed for producing chemicals. The production of synthesis gas (i.e., syngas, which is a mixture of CO and H_2) from CO_2 via reverse water-gas shift (RWGS) offers a path to decarbonizing the chemical industry, as a first step in obtaining syngas, which can be converted to a variety of products through Fischer-Tropsch synthesis (FTS) or methanol production reaction in a second step [3–5]. Temperature gap between both reactors (based on first and second steps) is significant. Based on thermodynamics, the RWGS reaction should run at 600–750 °C upstream, and the downstream unit at 250–400 °C for mentioned processes [6]. However, there is a growing interest in coupling these processes via tandem catalysis, which requires RWGS to be operated at intermediate temperatures, where methanation is a competing reaction.

RWGS reaction is a thermochemical hydrogenation of CO_2 to CO (Eq. (1)) and can be used to produce syngas with a desired H/C ratio, an

* Corresponding author.
E-mail address: m.duyar@surrey.ac.uk (M.S. Duyar).

https://doi.org/10.1016/j.jcou.2023.102606
Received 21 July 2023; Received in revised form 12 October 2023; Accepted 12 October 2023
Available online 19 October 2023

important parameter for downstream chemical synthesis. RWGS is thermodynamically favored at high temperatures (greater than 500 °C) and competes with the methanation reaction (Eq. (2)) that is thermodynamically favorable at low temperatures [7–9]. The low temperatures favoring methanation over RWGS present a challenge to commercialization of RWGS-based tandem catalysis technology, where downstream processes for utilizing syngas operate at much lower temperatures (200–300 °C for FTS) [10–12]. If sufficiently high selectivity over methanation can be obtained at low temperatures, this would open up commercial opportunities for RWGS to be implemented upstream of FTS, as well as for tandem catalytic schemes to be designed where RWGS is integrated into a reaction utilizing syngas and hence achieving process intensification through reaction coupling [9].

$$CO_2 + H_2 \leftrightarrow CO + H_2O \quad \Delta H^{\circ}_{298} = 41kJ/mol \tag{1}$$

$$CO_2 + 4H_2 \leftrightarrow CH_4 + 2H_2O \ \Delta H^{\circ}_{298} = -165kJ/mol \tag{2}$$

Nickel phosphide catalysts are effective in promoting CO_2 conversion due to their ability to facilitate the reduction of CO_2 to more useful chemicals [13,14]. In addition, nickel phosphide has shown successful catalytic performance on dry reforming of methane [15,16]. One of the main advantages of these catalysts is that they are highly stable under reaction conditions, which include high temperatures. Also, nickel phosphide catalysts are effective in the RWGS reaction because they have a high surface area and many active sites for catalysis. The effects of different nickel phosphide ratios and supports on the surface area were investigated, where the surface area of the supported Ni_2P-SiO_2 catalyst was found to be 4 times more than $Ni_{12}P_5$-CeAl and 3 times more than $Ni_{12}P_5$-Al_2O_3 [7].

While Ni metal is a well-established methanation catalyst, phosphidation of Ni can suppress methanation activity completely, with the choice of support playing a substantial role in catalytic performance as well [7]. In the present work, we explore the effects of Ni/P atomic ratio during synthesis on the Ni phosphide crystal structure, catalytic RWGS performance, and stability. Higher Ni/P ratios (12/5 and 2/1) produce high CO_2 conversions, high CO selectivities and high CO yields. Lower Ni/P ratios result in greater loss of phosphorus during the reduction and reaction stage. Moreover, silica-supported nickel phosphide catalysts with high Ni/P ratios can catalyze the RWGS reaction at temperatures as low as 300 °C showing CH_4 formation to be no longer a critical problem, and their activity increases with increasing temperature.

2. Materials and methods

2.1. Catalysts preparation

All catalysts used in this study were synthesized using the wet impregnation method [7]. Required amounts of nickel nitrate hexahydrate [$Ni(NO_3)_2.6\ H_2O$] and diammonium hydrogen phosphate [$(NH_4)_2.HPO_4$] were weighed and mixed for each catalyst. Deionized water was added to these mixtures. All the resulting mixed solutions were first stirred at room temperature and then concentrated under vacuum on a rotary evaporator. The resulting concentrated materials were then dried at 80 °C overnight and calcined at 500 °C for 2 h. A part of each prepared calcined sample was then reduced under an H_2 atmosphere (60 mL/min for 0.5 g of each catalyst). This protocol was carried out as follows; the temperature was raised from room temperature to 650 °C at a rate of 2 °C/min, and it was held constant at 650 °C for 2 h. Samples were then cooled to room temperature in Ar. Before exposure to air, samples were passivated in 3% O_2/Ar for at least 2 h at room temperature.

Catalysts were named Ni_aP_b-SiO_2, where a/b was the atomic ratio used for Ni to P for each catalyst. The Ni/P atomic ratios synthesized were 12/5, 2/1, 1/1 and 1/2, therefore, the catalysts were named $Ni_{12}P_5$-SiO_2, Ni_2P-SiO_2, NiP-SiO_2, and NiP_2-SiO_2, respectively.

2.2. Catalysts characterization

Synthesized catalysts were characterized using X-ray Diffraction (XRD), Temperature-Programmed Reduction (TPR), Inductively Coupled Plasma Mass Spectroscopy (ICP-MS), Particle Sizer, and X-ray Photoelectron Spectroscopy (XPS).

2.2.1. XRD

XRD analysis was performed with an X'Pert Pro PANalytical instrument at room temperature with Cu-K° (30 mA, 40 kV) in the 2-theta range of 10°– 80° and a step size of 0.05° with a step time of 450 s. XRD analysis was performed on freshly reduced catalysts, post-temperature scanning and post-stability test samples. Also, the average crystallite size (D_C) was estimated using the Scherrer formula (Eq. (3)).

$$D_C = \frac{K \times \lambda}{\beta \times \cos\theta} \tag{3}$$

Where K is a constant that depends on the shape of the crystallites (K = 0.9 in this study), λ is the wavelength of the X-rays used, β is the full width at half maximum (FWHM) of the diffraction peak in radians and θ is the diffraction angle [17].

The Scherrer equation uses XRD data and is based on the principle that the width of a diffraction peak is related to the size of the crystalline grains in the material [18]. The larger the grain size, the narrower the peak [19].

2.2.2. TPR

Hydrogen consumption of catalyst precursors was determined by H_2 Temperature-Programmed Reduction (H_2-TPR) to characterize the formation of Ni phosphide phases. H_2-TPR protocol was performed in a vertical fixed-bed quartz reactor under a mixture of 5 mL/min H_2 and 20 mL/min Ar. After the preparation of the quartz wool bed in the reactor, 50 mg of catalyst precursor was added, and the system was heated up to 920 °C at 10 °C/min. H_2 consumption data was recorded with an online mass spectrometer (Pfeiffer, OmniStar GSD 301).

2.2.3. ICP-MS

The concentrations of Ni, P, and Si were determined by ICP-MS using the iCAP 7200 ICP-OES Duo spectrometer from ThermoFisher Scientific following microwave digestion in an ETHOS EASY microwave digestion platform from Milestone. 10 mg of each sample was dissolved in 50 mL of solvent for analysis using the ICP-MS technique.

2.2.4. XPS

XPS measurements were carried out on SPECS spectrometer equipped with PHOIBOS 150 MCD analyzer working with fixed pass energy of 40 eV and 0.1 eV resolution for the studied zones. A non-monochromatic source of radiation, Al Kα radiation (1486.6 eV) working on 250 W and 12.5 kV voltage was used. The analytical chamber operated at ultra-high vacuum at around 10^{-10} mbar pressure. Prior to use, samples were pressed onto a thin disk. The XPS spectra were recorded at room temperature and the spectra were referenced to the Si 2p at 103.5 eV and fitted using CasaXPS software with a Gaussian–Lorentzian peak shapes and Shirley baselines. National Institute of Standards and Technology (NIST) XPS database was used to analyze the samples [20].

2.2.5. Powder particle size analysis

Powder particle sizes of selected samples were measured using a particle sizer (QicPic) and reported in Fig. S1.

2.3. Catalytic testing

RWGS reaction was performed in a vertical continuous fixed-bed reactor connected to the Advanced Optima Process Gas Analyser (ABB

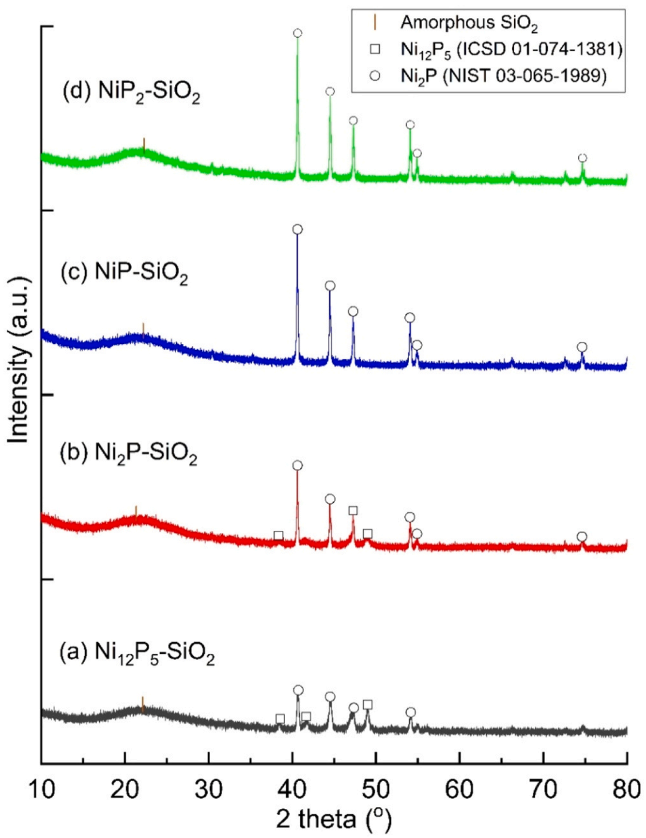

Fig. 1. XRD patterns for pre-reaction/reduced (a) $Ni_{12}P_5$-SiO_2, (b) Ni_2P-SiO_2, (c) NiP-SiO_2 and (d) NiP_2-SiO_2 catalysts.

AO2020), and the outlet volumetric percentages of CO_2, CO, H_2, and CH_4 were recorded. The reactor was a quartz-glass tube with an outer diameter of 12.7 mm and a length of 30 cm. 0.25 g of catalyst was placed on a quartz wool bed in the middle of the reactor. The reactor was heated with a tube furnace and the temperature inside was measured with a K-type thermocouple placed above the catalyst bed. To pre-reduce/re-activate the catalyst, hydrogen gas was passed, and the system was heated up to 650 ℃ from room temperature, and it was kept at this temperature for an hour. The system was then cooled to the testing temperature of 300 ℃ in N_2. Then, N_2 was replaced with a feed gas mixture of N_2:H_2:CO_2 = 5:4:1 and a total flow rate of 50 mL/min. The temperature of the system was increased from 300° to 800°C by the increment of 50 °C each time, and the amount of products obtained from RWGS reaction and the total flow rate of feed gases at each temperature were recorded after 25 min of steady-state reaction time. Stability tests were conducted at 550 °C for 24 h, with an H_2:CO_2 ratio of 4:1. Both stability and activity tests were performed at a constant weight-hourly space velocity (WHSV) of 12,000 mL g^{-1} h^{-1}. CO_2 conversion, CO selectivity, CH_4 selectivity, CO yield, and carbon balance were calculated for each catalyst using the Eqs. (4)–(8), respectively, based on the data obtained from the temperature screening and stability tests.

$$CO_2conversion(\%) = \frac{nCO_{2in} - nCO_{2out}}{nCO_{2in}} \times 100 \tag{4}$$

$$CO\ selectivity(\%) = \frac{nCO_{out}}{nCO_{out} + nCH_{4out}} \times 100 \tag{5}$$

$$CH_4selectivity(\%) = \frac{nCH_{4out}}{nCO_{out} + nCH_{4out}} \times 100 \tag{6}$$

$$CO\ yield(\%) = \frac{nCO_{out}}{nCO_{2in}} \times 100 \tag{7}$$

$$Carbon\ balance(\%) = \frac{nCO_{out} + nCO_{2out} + nCH_{4out}}{nCO_{2in}} \times 100 \tag{8}$$

Here, nCO_{2in} is the initial molar flow rate of CO_2 in the reactant mixture entering the system (kmol/min), and nCO_{out}, nCO_{2out} and nCH_{4out} are the molar amounts (in kmol/min) of CO, CO_2 and CH_4 in the product stream leaving the system, respectively.

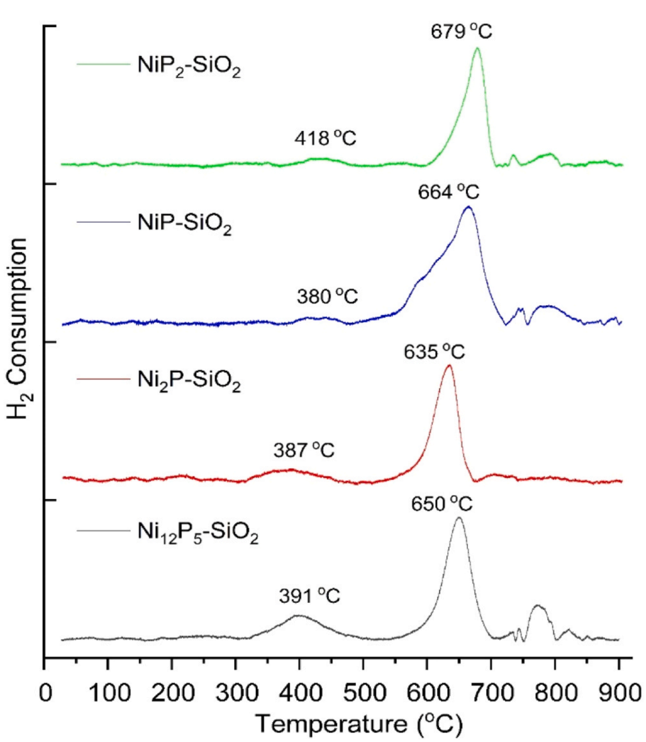

Fig. 2. H_2-TPR results (H_2 consumption) for calcined/pre-reduced samples.

3. Results and discussion

3.1. The effect of Ni/P ratio on crystal structure

XRD patterns of reduced (or pre-reaction) catalysts (using the protocol outlined in 2.1) are shown in Fig. 1, and detailed results are available in the Mendeley Data Repository [21]. The main phases observed across the range of catalysts were Ni_2P and $Ni_{12}P_5$ with the crystal structure showing a clear dependence on the synthesis Ni/P ratio. Amorphous SiO_2 was detected for all catalysts at diffraction angles 15–35° [7,22,23]. Ni_2P and $Ni_{12}P_5$ were the major phases observed for the pre-reaction XRD of the catalysts as per literature data [22]. XRD showed all observed species to be nickel-rich. For lower Ni/P atomic ratios (less than 1) or high P content, Ni_2P was shown to be the dominant phase (indicating that catalysts might have lost some of the phosphorous content during reduction [24]). Higher Ni/P ratios (greater than 1) or low P content showed $Ni_{12}P_5$ as well, in addition to the dominant Ni_2P phase (as observed in [24]). The results of Ni/P atomic ratios of 1 and 2 were almost identical to the previous findings [22]. Catalysts with a pure Ni_2P phase were obtained for the lower Ni/P ratios (0.5 and 1), while mixed Ni_2P and $Ni_{12}P_5$ structures were obtained for the catalysts with higher Ni/P ratios (2 and 2.4). W. Zhou et al. [25] found pure phases for Ni/P ratios of 2 and 2.4; Ni_2P phase in case of Ni/P atomic ratio of 2 and $Ni_{12}P_5$ phase in case of Ni/P atomic ratio of 2.4. Also, D. Lou et al. [26] observed the pure $Ni_{12}P_5$ phase for a Ni/P molar ratio of 2.4. M. H. Al Rashid [27] performed X-ray Absorption Near Edge Structure Spectra Analysis and showed that the Ni/P molar ratio of 1 produced Ni_2P, which was confirmed by the X-ray Absorption Edge and the Extended

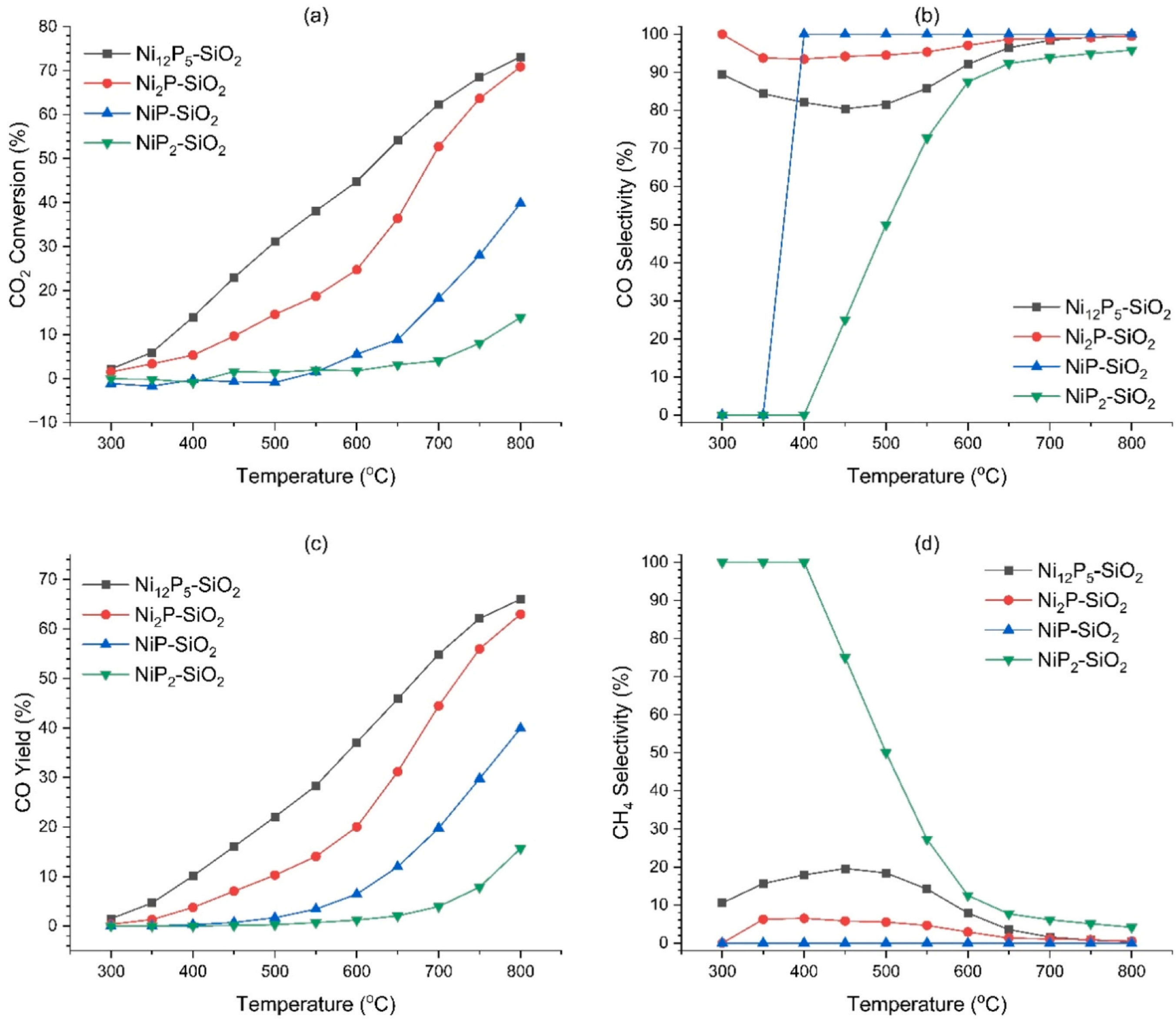

Fig. 3. (a) CO_2 conversion of each sample (b) CO Selectivity achieved by using each sample (c) CO yield achieved for each sample (d) CH_4 selectivity by using each sample catalyst (N_2:H_2:CO_2 =5:4:1, T = 300–800 °C, WHSV=12,000 mL g^{-1} h^{-1}).

X-ray Absorption Fine Structure Analysis using curve fitting. The Ni/P ratios of 2 and 3 resulted in $Ni_{12}P_5$ and Ni_3P phases, respectively.

Pre-reaction XRD examination of all the catalysts showed the presence of either the Ni_2P phase or the $Ni_{12}P_5$ phase. Diffraction peaks at 40.8°, 47.3°, 54.2°, 54.9° and 74.8° were observed, corresponding to the (111), (210), (300), (211), and (400) crystal planes of Ni_2P (JCPDS No. 03–0953) [7,28]. The peaks at 44.4°, 51.7° and 76.5° correspond to Ni, which were observed as well. The broad peak corresponding to 2-theta values between 20° and 25° indicated the presence of amorphous SiO_2. Diffraction peaks at 2-theta values of 33.2°, 38.4°, 46.1°, 46.7°, 47.3°, 48.1° and 48.9° were attributed to the crystal planes indicating successful synthesis of $Ni_{12}P_5$ (JCPDS no. 22–1190) [29,30]. All characteristic diffraction peaks of NiP_2 (JCPDS 21–0590) were observed, and the peaks at 28.34°, 32.85°, 36.86°, 40.52°, 47.14°, 55.92°, 58.64°, 61.25°, 63.87°, 76.08° and 78.43° matched well with (111), (200), (210), (211), (220), (311), (222), (320), (321), (331), and (420), respectively [5,31–33].

3.2. H_2-TPR analysis

For a better understanding of the redox properties of the catalysts and the interactions between the nickel phosphide phases and the support, the conversion of catalyst precursors (before reduction) to phosphides was investigated by H_2-TPR experiments. The hydrogen consumption profiles of the samples from room temperature to 920 ℃ are shown in Fig. 2, and experimental results are available online at Mendeley Data Repository [21]. H_2-TPR showed a typical small H_2 consumption peak between 380 and 420 ℃ for each silica-supported nickel phosphide calcined (pre-reduced) catalyst, corresponding to the initial reduction of bulk NiO, in accordance with previous studies [7,24]. Reductions of the nickel species in phosphate and P-O bonds because of the dissociation of H_2 on metallic Ni sites were observed with the highest peak between 630 and 680 ℃ [34–36]. According to O. Clause et al. [37], the reduction of PO_x/SiO_2 starts at about 800 ℃ and the completion temperature could reach up to about 1000 ℃ due to the thermally highly stable P-O bond. However, unlike previous studies, the reduction occurred at a lower temperature because of decomposition of H_2 on metallic Ni causing the PO_x/SiO_2 phase to be reduced more easily

[7]. In other words, the reduction temperature decreased due to the presence of metallic nickel in our nickel-phosphide catalysts [22].

Examining the H_2-TPR plots for all samples, two systematic trends were seen for samples with different Ni/P atomic ratios. Firstly, samples with lower P content showed more peaks and a complex overall reduction pattern than higher P samples. Secondly, all reduction peaks shifted to higher temperatures in samples with higher P contents [24]. Lower P contents contained more nickel compounds such as nickel oxide and nickel oxide-phosphates, resulting in different peaks due to their individual reduction. Since nickel oxides could be reduced more easily than the nickel species in phosphate and P-O bonds, peaks began to appear at lower temperatures [24].

Moreover, the reducibility was determined by analyzing the peak area of H_2-TPR profiles, which indicated the quantity of reducing agent (H_2) utilized (and usually the quantity of species in the solid phase undergoing reduction) during the reduction process within a specific temperature range [38,39]. H_2-TPR profile areas for each catalyst (mentioned in Table S1) were shown to be in following order: $Ni_{12}P_5$-SiO_2 > NiP-SiO_2 > Ni_2P-SiO_2 > NiP_2-SiO_2, indicating $Ni_{12}P_5$-SiO_2 profile area to be 2 times more than that of NiP_2-SiO_2.

3.3. Catalytic performance

Catalytic behavior for RWGS is reported in Table S2 (available in the supplementary information) and Fig. 3. Detailed activity results can be obtained from Mendeley Data Repository [21]. It was observed that the catalysts with lower Ni/P atomic ratios (1/1 and 1/2) were not active for RWGS at lower temperatures, and even at higher temperatures, they were less active as compared to the catalysts with higher Ni/P atomic ratios (2/1 and 12/5). $Ni_{12}P_5$-SiO_2 and Ni_2P-SiO_2 catalysts showed CO_2 conversion and CO selectivity even at lower temperatures as compared to NiP-SiO_2 and NiP_2-SiO_2 catalysts. Catalysts with greater Ni/P ratios exhibited a bigger increase in activity with increasing temperature than the catalysts with lower Ni/P ratios. However, methanation occurred to a very small extent for catalysts with higher Ni/P atomic ratios, which decreased with increasing temperatures. $Ni_{12}P_5$-SiO_2 had overall less CH_4 selectivity at a wider temperature range but slightly more as compared to that of Ni_2P-SiO_2 catalyst. Because of highly endothermic nature of RWGS and the very high conversions obtained with some of our catalysts, it should be noted that there was the possibility of cold spots formation [40] which might contribute to the activity data in Fig. 3. These spots within the catalytic reactor might create temperature gradients resulting from uneven heat distribution, possibly impacting mass and heat transfer, affecting reactant and product transport to and from the catalyst surface, potentially leading to different reaction pathways and selectivity. Controlling catalyst particle size could minimize heat and mass transfer limitations [40]. More importantly, it was necessary to constrain kinetic analysis to differential conditions of operation.

When comparing the activity data with H_2-TPR analysis, catalyst with highest reducibility (i.e., $Ni_{12}P_5$-SiO_2) showed the highest CO_2 conversion, while the catalyst with lowest reducibility (i.e., NiP_2-SiO_2) showed the lowest CO_2 conversion. Based on CO_2 conversion, CO selectivity, CO yield, and overall CH_4 selectivity at a wider temperature range, $Ni_{12}P_5$-SiO_2, i.e., the catalyst with the highest Ni/P atomic ratio, followed by Ni_2P-SiO_2 were found to be most suitable for RWGS. The overall suitability order based on the activity of the studied catalysts for the temperatures 300–800 °C was $Ni_{12}P_5$-SiO_2 > Ni_2P-SiO_2 > NiP-SiO_2 > NiP_2-SiO_2.

Site blocking effect (P on Ni), activity of distinct nickel phosphide phases ($Ni_{12}P_5$, Ni_3P and Ni_2P) and crystal structure might all be contributing to the high degree of suppression of methanation observed in these tests [7]. The combined presence of nickel phosphide and silica support in the catalyst might have also played a key role in suppressing methanation and improving CO selectivity [7].

U. Guharoy et al. [41] theoretically investigated the formation of methane during the RWGS process when nickel phosphide was used as a catalyst via the DFT method and proposed that the RWGS reaction over nickel phosphide catalysts occurred through a carbonate intermediate, which underwent further reactions to form CO or CH_4. Q. Zhang et al. [7] found that nickel phosphide catalysts were active and selective for the RWGS reaction and could produce CO and H_2 through the reduction of CO_2 and water, respectively. However, it was also found that nickel phosphide catalysts could also result in the formation of methane as a byproduct of the RWGS reaction, and it was suggested [7] that the formation of methane could be attributed to the presence of basic sites on the nickel phosphide catalysts and the intermediate carbonates, which could undergo further reactions to form CH_4. The support could also impact the dispersion and accessibility of the active sites on the nickel phosphide catalyst, affecting its catalytic activity and selectivity towards different products. SiO_2 support was shown to suppress the methanation activity of nickel phosphide catalysts [7,42]. The addition of SiO_2 led to a decrease in CO_2 adsorption, which in turn, lowered the availability of adsorbed CO_2 for methanation reaction [7]. SiO_2 support could also provide more acidic sites on the surface, which possibly favored the adsorption of CO_2 and inhibited methanation [42].

Iso-conversion selectivity analysis (Table S3) showed that both CO and CH_4 selectivities were different at CO_2 conversion ≈ 10% for all the catalysts indicative of intrinsic differences between the catalysts formed using different Ni/P atomic ratios. Therefore, activity was analyzed further in terms of activation energy in the next paragraph to give more insights about the impact of Ni/P atomic ratio on reaction pathways.

Apparent activation energy (E_a) of CO_2 reduction for each catalyst was measured (and shown in Fig. 4) for conditions and temperature ranges associated with CO_2 conversion < 25% (differential conditions). At some point, where CO_2 conversion > 25%, transport limitations would have been encountered, hence the Arrhenius plots for catalysts were limited to CO_2 conversions < 25%. E_a based on CO_2 conversion for $Ni_{12}P_5$-SiO_2 (T = 300–450 °C) was 55 kJ/mol, higher than that of Ni_2P-SiO_2 (i.e., 39 kJ/mol, T = 300–600 °C) as shown in Fig. 4. NiP-SiO_2 catalyst had a very high E_a for CO_2 conversion (83.74 kJ/mol), also at high temperatures (600–700 °C), as shown in Fig. 4. NiP_2-SiO_2 catalyst also showed a high CO_2 conversion E_a (78.2 kJ/mol) even at very high temperatures (600–800 °C) as given in Table S4 and Fig. 4. Also, Arrhenius data of NiP_2-SiO_2 catalyst displayed deviation from linearity possibly because of catalyst's restructuring at lower CO_2 conversions (450–800 °C) as shown in Fig. S2. Lower CO_2 conversion activation energies for catalysts with higher Ni/P atomic ratios were reflected in

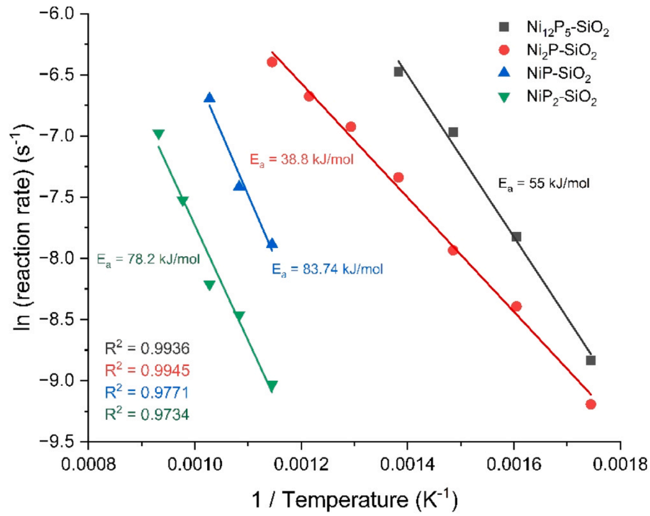

Fig. 4. Arrhenius plots of $Ni_{12}P_5$-SiO_2 (300–450 °C), Ni_2P-SiO_2 (300–600 °C), NiP-SiO_2 (600–700 °C) and NiP_2-SiO_2 (600–800 °C) catalysts for RWGS CO_2 conversions < 25%.

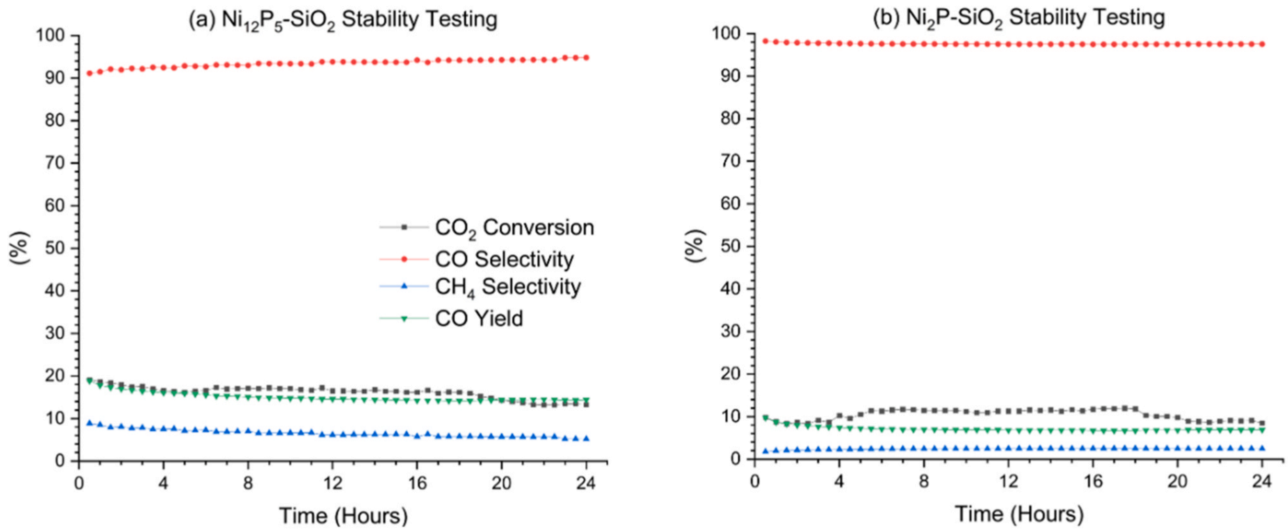

Fig. 5. 24-h RWGS stability test results for: (a) $Ni_{12}P_5$-SiO_2 and (b) Ni_2P-SiO_2 catalysts (N_2:H_2:CO_2 =5:4:1, T = 550 °C, WHSV=12,000 mL g^{-1} h^{-1}).

activity presented in Fig. 3. CO_2 conversion activation energies for some of the catalysts developed as a part of this study ($Ni_{12}P_5$-SiO_2 and Ni_2P-SiO_2) were lower than kinetically controlled activation energies of Re-SiO_2 (84.5 kJ/mol, 360–440 °C), Pt-zeolite (60 kJ/mol, 360–440 °C), Pt-SiO_2 (60.1 kJ/mol, 360–440 °C), 5.6–20 wt% of Ni on SiO_2 (83–94 kJ/mol, 325–400 °C), Ni0.1Mo (77.7 kJ/mol, 320–400 °C) and Ni1Mo (74.4 kJ/mol, 320–400 °C) under differential conditions [43, 44]. Moreover, observed activation energies were also comparable to those of Fe (50 kJ/mol) and Pt0.5Re (48.6 kJ/mol, 360–440 °C) [45, 46]. Heat and mass transfer limitations were practically excluded because the reported apparent activation energies under differential conditions in this study were in the range of kinetically controlled reaction activation energies. Nitrogen was added to dilute the (feed gases) stream so it kept the temperature stable, and a low catalyst volume was used.

According to Table S2, carbon balance was reduced with increasing temperatures (as low as 94.9% and 96% at 550 ℃) for $Ni_{12}P_5$-SiO_2 and Ni_2P-SiO_2 catalysts, while for NiP-SiO_2 and NiP_2-SiO_2 catalysts, it was close to 100%. Less than 100% carbon balance suggested the presence of some unaccounted carbon-containing species (gas phase products other than methane or CO) in the product stream and/or deposition of carbon species on the catalysts [8]. Slightly negative CO_2 conversions at lower temperatures for NiP-SiO_2 and NiP_2-SiO_2 catalysts (as shown in Table S2 and Fig. 3(a)) were attributed to fluctuations in mass flow at zero % conversion.

3.4. *Stability Test*

Stability tests were carried out for 24 h with the $Ni_{12}P_5$-SiO_2 and Ni_2P-SiO_2 catalysts in RWGS process with N_2:H_2:CO_2 ratio of 5:4:1and a WHSV of 12,000 mL g^{-1} h^{-1} at 550 °C. CO_2 conversion, CO selectivity, CH_4 selectivity, and CO yield obtained for these stability tests are shown in Fig. 5. Complete stability test results can be found at Mendeley Data Repository [21]. Tests aimed to evaluate the performance of these catalysts, which were known for their excellent ability to suppress side reactions in RWGS, in maintaining their efficiency over a prolonged period.

For the $Ni_{12}P_5$-SiO_2 catalyst, the CO_2 conversion showed a small decline from 19% to 13% over the 24-hour duration, indicating a relatively stable conversion and a robust performance of the catalyst. Additionally, while the CO yield decreased from 19% to 14%, the CO selectivity remained high, fluctuating between 91% and 95% (with more than 90% selectivity observed most of the time). CH_4 selectivity decreased during the test. This suggested that the $Ni_{12}P_5$-SiO_2 catalyst was effective in selectively producing CO and suppressing the formation of other byproducts (such as CH_4), even after 24 h of use.

For the Ni_2P-SiO_2 catalyst, the CO_2 conversion remained relatively stable, between 8.5% and 12%, over the 24-hour duration. The CO yield decreased from 10% to 7% in the first 6 h but then remained relatively stable for the rest of the time. This could mean that the catalyst was losing some of its efficiency over time but still maintaining its performance. This could also be a result of changes in reaction conditions or the catalyst deactivating and then partially recovering over the course of the test. The CO selectivity ranged between 97% and 99%. The CH_4 selectivity remained very low, between 1.4% and 2.1%, throughout the test, which indicated that the Ni_2P-SiO_2 catalyst was highly selective in producing CO and it suppressed the formation of byproducts such as CH_4, which was noteworthy.

Stability tests demonstrated that both $Ni_{12}P_5$-SiO_2 and Ni_2P-SiO_2 catalysts showed promising performance in suppressing side reactions and selectively producing CO in the RWGS process. The $Ni_{12}P_5$-SiO_2 catalyst was effective in maintaining high CO selectivity over the 24-hour test, while the Ni_2P-SiO_2 catalyst showed relatively stable CO_2 conversion and CO yield. Also, when activity test results were compared with stability test results; less CO_2 conversion, decreased CO yield and importantly less methanation were obtained for both the catalysts at 550 °C during stability tests, indicating that the results were difficult to reproduce, because factors such as Ni/P atomic ratios, support, conditions, synthesis method, etc., might have highly affected the performance of silica supported nickel phosphide catalysts. For instance, activity tests involved catalyst activation in an H_2 atmosphere at 650 °C for an hour, then cooling down to 300 °C in N_2, followed by a gradual temperature increase up to 800 °C, revealing fluctuations in total flow rate. At 550 °C, $Ni_{12}P_5$-SiO_2 exhibited 7.67% CO_2 volume and 46.91 mL/min total flowrate during activity testing, while Ni_2P-SiO_2 showed 9.5% CO_2 volume and 49.58 mL/min total flowrate, as shown in Fig. S3 (available in the supplementary information of this paper). On the other hand, after activation in H_2, the system was cooled down to 550 °C (rather than 300 °C as in case of activity testing), stability tests were then conducted at 550 °C, yielding an average CO_2 volume of 9.59% and a 50.19 mL/min average total flowrate for $Ni_{12}P_5$-SiO_2, and 10.30% CO_2 volume and 49.14 mL/min average total flowrate for Ni_2P-SiO_2 (as indicated in Fig. S3). The CO_2% volume differences between activity and stability tests were 25% for $Ni_{12}P_5$-SiO_2 and 8% for Ni_2P-SiO_2, with total flow rate differences of 7% and 1%, respectively. Hence variations between activity and stability test results were likely attributed to flow rates and the catalysts' operational history. However, both activity and stability tests showed that $Ni_{12}P_5$-SiO_2 was a better catalyst

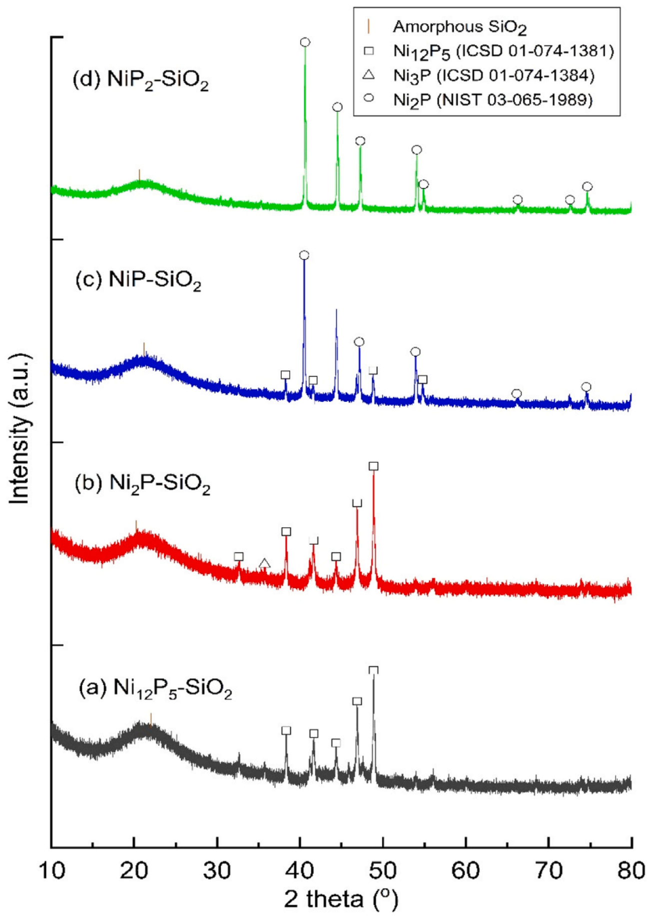

Fig. 6. XRD patterns for post-reaction (a) $Ni_{12}P_5$-SiO_2, (b) Ni_2P-SiO_2, (c) NiP-SiO_2 and (d) NiP_2-SiO_2 catalysts.

(when compared with the other studied catalysts) for RWGS over the 300–800 °C temperature range.

3.5. *Post-reaction and post-stability XRD analysis*

XRD patterns for post-reaction samples are shown in Fig. 6. XRD analysis results for post-reaction and post-stability test samples are available at the Mendeley Data Repository [21]. When compared with XRD patterns of pre-reaction samples as shown in Fig. 1, catalysts had become more crystalline after RWGS (as shown in Fig. 6) due to prolonged high-temperature exposure. Phase transitions for each catalyst because of RWGS were detected using XRD analysis. The results are summarized in Table 1. All catalysts showed the presence of amorphous silica in their post-reaction XRD patterns [7,22]. The sample with the lowest Ni/P atomic ratio showed only the Ni_2P phase when analyzed via XRD after the reaction. Almost similar XRD patterns were observed for the NiP_2-SiO_2 catalyst. Post-reaction XRD characterisation of NiP-SiO_2 showed some presence of the $Ni_{12}P_5$ phase as well, however, the dominant phase was Ni_2P. Pre-reaction XRD of the same catalyst (NiP-SiO_2) with a Ni/P atomic ratio of 1 showed only the Ni_2P phase. For high Ni/P atomic ratios (2/1 and 12/5), the dominant phase was $Ni_{12}P_5$, while only a few small peaks matched with the Ni_3P phase (a small Ni_3P peak was visible in the case of Ni/P atomic ratio of 2, while Ni_3P peaks were very small and invisible in the case of Ni/P atomic ratio of 12/5, as shown in Fig. 6). In conclusion, post-reaction XRD characterization of Ni_2P-SiO_2 and $Ni_{12}P_5$-SiO_2 catalysts dominantly showed the $Ni_{12}P_5$ phase.

The synthesis Ni/P atomic ratio influenced the formation of different nickel phosphide phases and their subsequent properties, such as crystal structure, composition, and activity. XRD analysis showed the transformation of the Ni_2P phase during the reaction to the $Ni_{12}P_5$ phase (Fig. 6) for catalysts with Ni/P atomic ratios of 1, 2 and 2.4. A slight transformation to Ni_3P in the case of higher Ni/P ratios (2 and 2.4) was also observed. These transformations could be because the activity temperatures (up to 800 °C) were higher than the reduction temperature (650 °C) [7]. The H_2-TPR results indicated in Fig. 2 that the reduction of nickel phosphate proceeded until it reached a temperature of 750 °C. As a result, these catalysts underwent further reduction under a constant H_2 input and an elevated temperature of 750 °C. Z. Ma et al. [47] also concluded that the phase transition from Ni_2P to $Ni_{12}P_5$ or another phase (such as Ni_3P) occurred when there was less phosphorous. Moreover, as the temperature increased, there was a greater tendency for the formation of $Ni_{12}P_5$ and Ni_3P phases. It should be noted that atomic ratio was not the only factor affecting the formation of a specific nickel phosphide phase. Factors such as synthesis method, temperature, flow rates, reaction time, and other operating conditions could have also played their role in determining the specific phase that was formed during the synthesis of nickel phosphide catalysts.

Previous studies (on RWGS [7], guaiacol hydrodeoxygenation [22], deoxygenation for fatty acid conversion [25], photothermal RWGS [26] and non-oxidative coupling of methane reaction [27]) indicated the presence of Ni_3P, Ni_2P, and $Ni_{12}P_5$ phases on silica-supported nickel phosphide catalysts. Ni/P = 1, 2, and 3 silica-supported samples showed Ni_2P, $Ni_{12}P_5$, and Ni_3P as the major phases, respectively, for Guaiacol hydrodeoxygenation [22], and lifetime tests showed the highest deactivation rate (~78%) for Ni/P = 1 (i.e., Ni_2P phase). Coking (formation of carbonaceous deposits on the catalyst surface) and phosphide leaching (dissolution of phosphides into the liquid or gas phase, i.e., loss of P) were identified as causes of deactivation. These phenomena might have also occurred in nickel phosphide catalysts used for RWGS, leading to similar deactivation patterns in the current study. The $Ni_{12}P_5$ phase demonstrated superior activity compared to the Ni_2P phase in alcohol oxidation [48] and fatty acid deoxygenation [25].

Among all reported nickel phosphide phases (Ni_2P, Ni_3P, and $Ni_{12}P_5$) in this work, $Ni_{12}P_5$ showed the highest CO_2 conversion and CO selectivity for RWGS reaction. Higher activity and selectivity of $Ni_{12}P_5$ for the RWGS reaction were due to the combination of its crystal structure and

Table 1
Phase transition and crystallite size detected through XRD for each catalyst.

Catalysts	Pre-reaction					Post-reaction				
	Amorphous SiO_2	Ni_3P	$Ni_{12}P_5$	Ni_2P	Crystallite Size (nm)	Amorphous SiO_2	Ni_3P	$Ni_{12}P_5$	Ni_2P	Crystallite Size (nm)
$Ni_{12}P_5$-SiO_2	✓	×	✓	✓ (Dominant)	2.2	✓	✓	✓ (Dominant)	×	2.8
Ni_2P-SiO_2	✓	×	✓	✓ (Dominant)	3.9	✓	✓	✓ (Dominant)	✓	4.1
NiP-SiO_2	✓	×	×	✓ (Dominant)	4.2	✓	×	✓	✓ (Dominant)	4.1
NiP_2-SiO_2	✓	×	×	✓ (Dominant)	4.2	✓	×	×	✓ (Dominant)	4.2

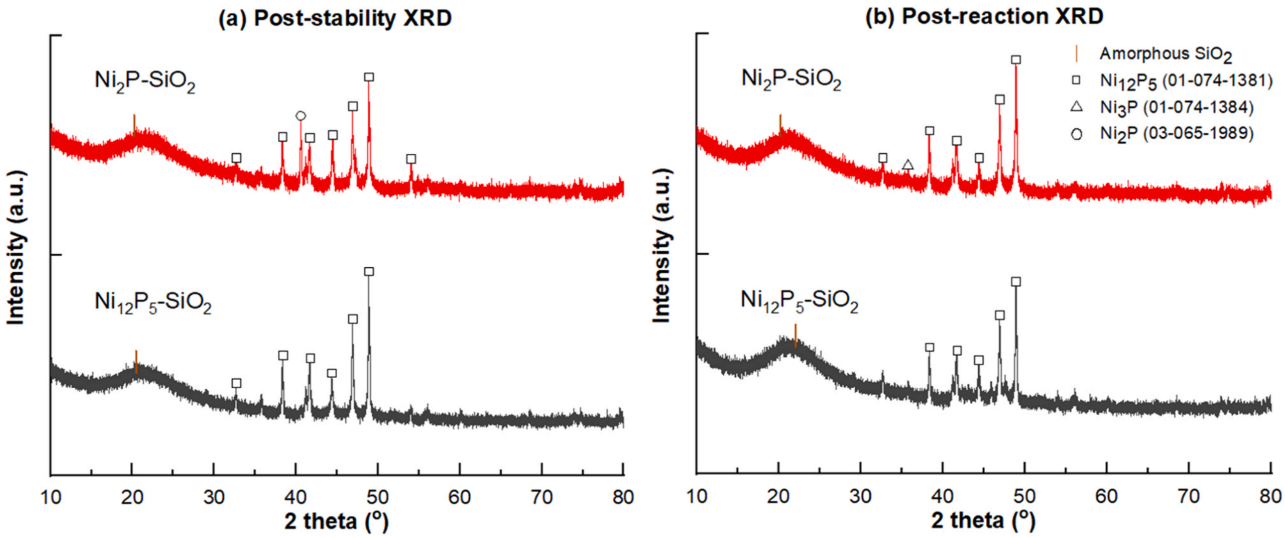

Fig. 7. (a) Post-stability and (b) post-reaction XRD patterns for $Ni_{12}P_5$-SiO_2 and Ni_2P-SiO_2 catalysts.

Table 2
Elemental composition of catalysts detected at different stages using ICP-MS analysis.

Sample	Calculated			Calcined			Pre-reaction (reduced)			Post-reaction		
	wt%		Ni/P atomic ratio	wt%		Ni/P atomic ratio	wt%		Ni/P atomic ratio	wt%		Ni/P atomic ratio
	Ni	P		Ni	P		Ni	P		Ni	P	
NiP_2-SiO_2	15	15.83	0.5001	10.22	11.22	0.4807	9.83	7.27	0.7135	11.48	6.97	0.8692
NiP-SiO_2	15	7.92	0.9995	13.02	7.03	0.9774	10.97	4.16	1.3916	8.42	3.33	1.3344
Ni_2P-SiO_2	15	3.96	1.9989	12.85	3.33	2.0364	11.89	3.08	2.0372	11.57	3.09	1.9760
$Ni_{12}P_5$-SiO_2	15	3.30	2.3987	13.89	3.04	2.4112	13.11	2.82	2.4533	10.87	2.38	2.4102

the presence of Ni-P bonds in its structure, leading to better electronic conductivity, and more efficient activation of H_2 [49–51]. The presence of negatively charged P in $Ni_{12}P_5$ could trap protons similar to hydrogenase, making it a promising catalyst for hydrogen evolution reactions as well. Crystalline structure of Ni_2P phase made the catalyst more conducive to promoting the RWGS reaction, resulting in high conversion and high selectivity, while Ni_3P phase (which showed its presence in post-reaction XRD of Ni_2P-SiO_2 and $Ni_{12}P_5$-SiO_2 catalysts) resulting from further reduction of $Ni_{12}P_5$ phase at high temperature and long-term run, could promote both methanation and RWGS reactions [7].

Post-reaction XRD patterns and post-stability XRD patterns for $Ni_{12}P_5$-SiO_2 and Ni_2P-SiO_2 are shown in Fig. 7. Post-stability XRD pattern of $Ni_{12}P_5$-SiO_2 showed the $Ni_{12}P_5$ phase, which was similar to what was observed in the post-reaction XRD of this catalyst. Post-stability XRD of Ni_2P-SiO_2 showed most peaks (including the dominant one) of the $Ni_{12}P_5$ phase (same as in the case of post-reaction XRD of this catalyst), however, a slight Ni_2P phase was also observed in post-stability XRD pattern of this catalyst. Ni_2P phase formation resulted from the higher temperatures and longer reaction times, promoting reactive P generation and conversion to thermodynamic product [52]. Overall, the same dominant phases were observed in post-reaction and post-stability XRD analysis for both catalysts.

The estimated crystal sizes of the catalysts calculated using Scherrer equation, before and after the reaction are given in Table 1. The estimated particle size increased with decreasing Ni/P ratio. The estimated Ni crystallite size of $Ni_{12}P_5$ calculated from the Scherrer equation was the smallest compared to the others, and it was calculated to be ~2 nm. The smaller particle size signified a higher degree of dispersion in that sample, potentially contributing to its better catalytic activity [53–55]. No changes were observed in the post-reaction Ni particle sizes compared to the pre-reaction ones apart from the $Ni_{12}P_5$ sample, which exhibited a minor, almost negligible, increase.

3.6. Pre- and Post-reaction ICP-MS Analysis

The ICP-MS analysis results (available at Mendeley Data Repository [21]) for the elemental compositions of the catalysts at different stages of the RWGS process are presented in Table 2. The calculated Ni loading for each catalyst was 15 wt%, but the ICP-MS analysis showed lower loadings for calcined samples. For catalysts with Ni/P atomic ratio ≥ 1, Ni wt% decreased further after reduction and passivation (pre-reaction stage), and this trend continued until the post-reaction stage. However, for NiP_2-SiO_2 catalyst, Ni wt% increased between the pre-reaction and post-reaction stages. The calculated P wt% for the studied catalysts ranged from 3.3 wt% to 15.83 wt% and the ICP analysis showed a decrease in P content from calcined to post-reaction samples.

Loss of phosphorous was observed for NiP_2-SiO_2 and NiP-SiO_2 catalysts with high P content, and this effect was more pronounced during the reduction stage. As the Ni/P atomic ratio increased, the phosphorous loss effect became more significant [24]. Therefore, the loss of P content resulted in the appearance of Ni_2P phases for NiP_2-SiO_2 and NiP-SiO_2 catalysts as shown by XRD characterization. The loss of P was negligible for $Ni_{12}P_5$-SiO_2 and Ni_2P-SiO_2 catalysts with low P content. Q. Sheng et al. [56] demonstrated that during the TPR of nickel phosphate, the formation of PH_3 and P^{n+} species in the gas flows increased significantly above 510 °C. PH_3 was generated by the reduction of phosphate precursors in H_2, and the reaction of PH_3 with H_2O produced P^{n+} species, which were involved in the formation of phosphide phases. The generation of PH_3 and P^{n+} species from continuous H_2 reduction in RWGS could have possibly contributed to the disproportionation of the phosphide. However, the extended testing showed stabilized performance, suggesting that the loss of P might not have been continuous.

Overall, the results indicated that the elemental composition of the

Table 3
Pre- and post-reaction surface composition (XPS) for $Ni_{12}P_5$-SiO_2 and Ni_2P-SiO_2.

Catalysts, %at	Ni	P	Ni/P	Si	O	Si/O	C
Pre-reaction $Ni_{12}P_5$-SiO_2	3.0	1.6	1.9	28.0	60.1	0.47	7.3
Pre-reaction Ni_2P-SiO_2	2.9	1.9	1.5	27.0	58.9	0.46	9.3
Post-reaction $Ni_{12}P_5$-SiO_2	2.5	1.4	1.8	30.2	62.3	0.48	3.6
Post-reaction Ni_2P-SiO_2	2.1	1.5	1.4	30.2	62.5	0.48	3.7

catalysts changed due to various factors such as reduction, phosphorous loss, and RWGS reaction. The differences between the calculated Ni loadings and the ICP analysis results suggested that the catalysts might have undergone some changes during synthesis or the reaction. The observed phosphorous loss highlighted the importance of carefully selecting the Ni/P atomic ratio and the support material to optimize the performance and stability of silica-supported nickel phosphide catalysts.

3.7. Pre- and post-reaction XPS analysis

In the survey spectra, the elements of the samples, Si, O, Ni and P, were detected, as well as small concentrations of carbon, typical of environmental contamination (adventitious carbon contamination). Ni/P and Si/O (typically for the silica support) ratios in the pre-reaction and post-reaction samples remained almost constant as in Table 3.

Ni 2p and P 2p regions observed via XPS are shown in Fig. 8 and other XPS-based results are demonstrated via Table 3 (surface composition) and Table 4 (P species) [57–60]. The Ni 2p region exhibited characteristic peaks for oxidized nickel, Ni 2p3/2 at 854.4 eV and Ni 2p1/2 at 872.5 eV, along with their respective satellites. Additionally, another doublet recorded at lower values, 851.0 and 868.3 eV, indicated the presence of reduced nickel Niδ+ . These peaks were related to the peak recorded in the P 2p region at 129.6 eV. The value was lower than that of elemental phosphorus (130.3 eV), indicating the presence of Pδ-. Therefore, it was concluded that there was an electron transfer from nickel to phosphorus, resulting in the presence of a Ni_xP_y, and peaks at these values in P spectra were assigned to the Ni_xP_y phases (Ni_2P and $Ni_{12}P_5$) as shown by XRD analysis [7]. As for the other phosphorus peak at 133.5 eV, it was characteristic of oxidized phosphorus as $(PO_4)^{3-}$. Both samples showed that the concentration of both nickel and phosphorus decreased slightly after the reaction, but the Ni/P ratio remained practically constant.

Although it was difficult to obtain a relation between oxidized phosphorus and the P in the alloy due to the presence of Ni 3s region, here these parameters were recorded as given in Table 4. The rest of the zones were not of interest; the Si 2p peak was used for charge correction, and the O 1s peak was from silicon oxide.

All three characterizations; XRD, ICP-MS and XPS showed Ni-rich phases in catalysts, hence showing remarkable structural consistency for $Ni_{12}P_5$-SiO_2 and Ni_2P-SiO_2 catalysts. Elemental composition for bulk catalysts measured via ICP-MS showed high Ni/P atomic ratios (comparable to theoretical values), while XPS determined Ni/P ratios at catalysts' surfaces which were shown to be less than those detected via ICP-MS, indicating a relatively phosphorous rich surface and a nickel-

Table 4
P species detected in pre- and post-reaction samples via XPS for $Ni_{12}P_5$-SiO_2 and Ni_2P-SiO_2.

Catalysts, %at	$(PO_4)^{3-}$	Ni_xP_y
Pre-reaction $Ni_{12}P_5$-SiO_2	38.8	61.2
Pre-reaction Ni_2P-SiO_2	45.4	54.6
Post-reaction $Ni_{12}P_5$-SiO_2	38.5	61.5
Post-reaction Ni_2P-SiO_2	51.1	48.9

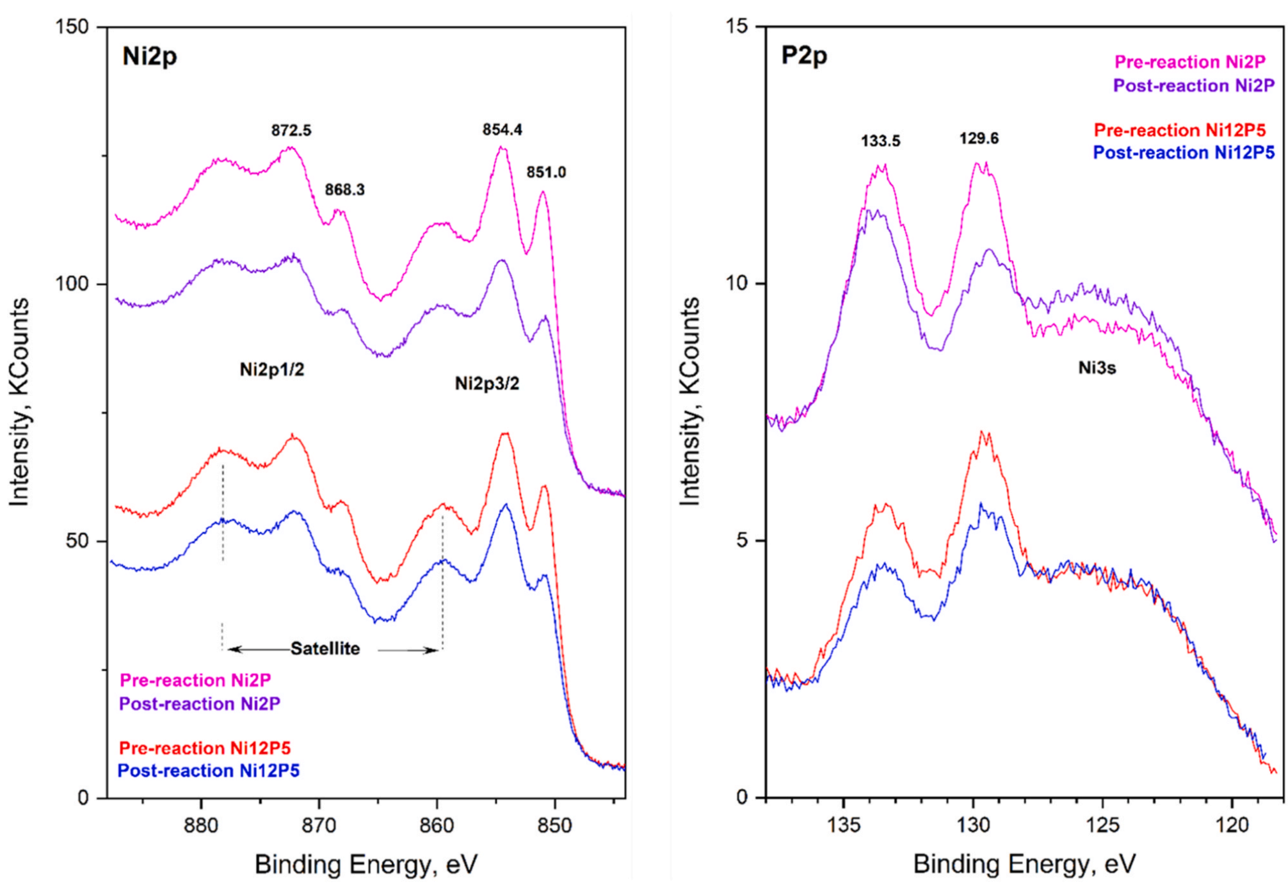

Fig. 8. XPS Ni2p spectra and P2p spectra.

rich core.

4. Conclusion and future recommendations

This research unveils the untapped potential of nickel phosphide catalysts for the RWGS reaction, and investigated the four catalysts, namely $Ni_{12}P_5$-SiO_2, Ni_2P-SiO_2, NiP-SiO_2, and NiP_2-SiO_2. Nickel phosphide catalysts prepared herein demonstrated high selectivity to CO and showed suppression of the competing methanation reaction, even at high H_2/CO ratios. CO_2 conversion, CO selectivity, and CO yield achieved by $Ni_{12}P_5$-SiO_2 and Ni_2P-SiO_2 were notable. $Ni_{12}P_5$-SiO_2 showed 73% CO_2 conversion and 66% CO yield at 800 °C, and 80–100% CO selectivity, whereas Ni_2P-SiO_2 showed 70% CO_2 conversion and 63% CO yield at 800 °C, and 93–100% CO selectivity. These two catalysts, particularly $Ni_{12}P_5$-SiO_2, exhibited superior RWGS activity to other catalysts even at lower temperatures ranging from 300 °C to 500 °C, which might be important for coupling to downstream or liquid fuel synthesis via Fischer Tropsch Synthesis. The overall catalyst suitability order for RWGS reaction based on the activity for the studied catalysts for the temperature range of 300–800 °C and stability testing of selected catalysts at 550 °C is $Ni_{12}P_5$-SiO_2 > Ni_2P-SiO_2 > NiP-SiO_2 > NiP_2-SiO_2. Support and Ni/P atomic ratio in each catalyst affect site blocking effects, and the formation of nickel phosphide phases (such as Ni_2P, $Ni_{12}P_5$ and Ni_3P; where $Ni_{12}P_5$ is proposed to be most active and stable Ni-P phase) observed via XRD characterization. Adjusting Ni/P atomic ratios allows for fine-tuning the catalytic activity of nickel phosphide catalysts in RWGS reactions. Also, higher Ni/P atomic ratios within the catalysts effectively suppress the undesired methanation while simultaneously enhancing the CO selectivity. RWGS activity at low temperatures and a high degree of suppression of the competing methanation reaction capability of nickel phosphide catalysts present a promising ground for future research by CO_2 valorization community on relatively less explored use of nickel phosphide RWGS process in tandem catalysis to develop cleaner and more efficient energy conversion processes.

CRediT authorship contribution statement

Gul Hameed: Investigation, Formal analysis, Visualization, Writing – original draft preparation. **Ali Goksu**: Investigation, Formal analysis, Visualization, Writing- Original draft preparation. **Loukia-Pantzechroula Merkouri**: Investigation, Writing – review & editing. **Anna Penkova**: Investigation. **Tomas Ramirez Reina**: Writing – review & editing, Methodology, Supervision. **Sergio Carrasco Ruiz**: Writing – review & editing, Investigation. **Melis Seher Duyar**: Conceptualization, Supervision, Writing – review & editing, Methodology, Project administration, Funding acquisition.

Declaration of Competing Interest

The authors declare that they have no known competing financial interests or personal relationships that could have appeared to influence the work reported in this paper.

Data Availability

Experimental results can be found at https://data.mendeley.com/datasets/ccxtpdyhfj/1, hosted at Mendeley Data [21]. Table S1, Table S2, Table S3, Table S4, Figure S1, Figure S2 and Figure S3 can be found in the Supplementary Information file.

Acknowledgements

Financial support for this work was provided by the Royal Society of Chemistry Research Enablement Grant (E21-7122134129).

Appendix A. Supporting information

Supplementary data associated with this article can be found in the online version at doi:10.1016/j.jcou.2023.102606.

References

[1] E.J. Nelson, et al., Climate change's impact on key ecosystem services and the human well-being they support in the US, Front Ecol. Environ. vol. 11 (9) (2013) 483–893.

[2] J.E. Walsh, et al., Extreme weather and climate events in northern areas: a review, Earth Sci. Rev. vol. 209 (2020), 103324, https://doi.org/10.1016/j.earscirev.2020.103324.

[3] A. Galadima, O. Muraza, Catalytic thermal conversion of CO_2 into fuels: perspective and challenges, Renew. Sustain. Energy Rev. vol. 115 (2019), 109333, https://doi.org/10.1016/j.rser.2019.109333.

[4] P. Gao, et al., Direct conversion of CO_2 into liquid fuels with high selectivity over a bifunctional catalyst, Nat. Chem. vol. 9 (10) (2017) 1019–1024, https://doi.org/10.1038/nchem.2794.

[5] Y. Ding, B.-Q. Miao, Y.-C. Jiang, H.-C. Yao, X.-F. Li, Y. Chen, Polyethylenimine-modified nickel phosphide nanosheets: interfacial protons boost the hydrogen evolution reaction, J. Mater. Chem. A Mater. vol. 7 (22) (2019) 13770–13776, https://doi.org/10.1039/C9TA04283K.

[6] J. Gandara-Loe, Q. Zhang, J.J. Villora-Picó, A. Sepúlveda-Escribano, L. Pastor-Pérez, T. Ramirez Reina, Design of full-temperature-range RWGS catalysts: impact of alkali promoters on Ni/CeO2, Energy Fuels vol. 36 (12) (2022) 6362–6373, https://doi.org/10.1021/acs.energyfuels.2c00784.

[7] Q. Zhang, et al., Ni-Phosphide catalysts as versatile systems for gas-phase CO_2 conversion: impact of the support and evidences of structure-sensitivity, Fuel vol. 323 (2022), 124301, https://doi.org/10.1016/j.fuel.2022.124301.

[8] Q. Zhang, M. Bown, L. Pastor-Pérez, M.S. Duyar, T.R. Reina, CO_2 conversion via reverse water gas shift reaction using fully selective mo–p multicomponent catalysts, Ind. Eng. Chem. Res vol. 61 (34) (2022) 12857–12865, https://doi.org/10.1021/acs.iecr.2c00305.

[9] R.M. Bown, M. Joyce, Q. Zhang, T.R. Reina, M.S. Duyar, Identifying commercial opportunities for the reverse water gas shift reaction, Energy Technol. vol. 9 (11) (2021) 2100554.

[10] L. Yang, L. Pastor-Pérez, J.J. Villora-Pico, S. Gu, A. Sepúlveda-Escribano, T. R. Reina, CO_2 valorisation via reverse water-gas shift reaction using promoted Fe/CeO2-Al2O3 catalysts: Showcasing the potential of advanced catalysts to explore new processes design, Appl. Catal. A Gen. vol. 593 (2020), 117442, https://doi.org/10.1016/j.apcata.2020.117442.

[11] M. Zhu, Q. Ge, X. Zhu, Catalytic reduction of CO_2 to CO via reverse water gas shift reaction: recent advances in the design of active and selective supported metal catalysts, Trans. Tianjin Univ. vol. 26 (3) (2020) 172–187, https://doi.org/10.1007/s12209-020-00246-8.

[12] R. Yamano, S. Ogo, N. Nakano, T. Higo, Y. Sekine, Non-conventional low-temperature reverse water–gas shift reaction over highly dispersed Ru catalysts in an electric field, EES Catal. vol. 1 (2) (2023) 125–133.

[13] H.Y. Zhao, D. Li, P. Bui, S.T. Oyama, Hydrodeoxygenation of guaiacol as model compound for pyrolysis oil on transition metal phosphide hydroprocessing catalysts, Appl. Catal. A Gen. vol. 391 (1) (2011) 305–310, https://doi.org/10.1016/j.apcata.2010.07.039.

[14] Z. Yu, et al., Ni 3 P as a high-performance catalytic phase for the hydrodeoxygenation of phenolic compounds, Green. Chem. vol. 20 (3) (2018) 609–619.

[15] Y. Shi, et al., Impact of nickel phosphides over Ni/SiO2 catalysts in dry methane reforming, Catal. Lett. (2022), https://doi.org/10.1007/s10562-022-04199-6.

[16] M. González-Castaño, et al., Nickel phosphide catalysts as efficient systems for CO_2 upgrading via dry reforming of methane, Catalysts vol. 11 (4) (2021), https://doi.org/10.3390/catal11040446.

[17] V.S. Vinila, J. Isac, Chapter 14 - Synthesis and structural studies of superconducting perovskite GdBa2Ca3Cu4O10.5+δ nanosystems, in: S. Thomas, N. Kalarikkal, A.R. B.T.-D. Abraham Fabrication, Characterization of Multifunctional Nanomaterials (Eds.), Micro and Nano Technologies, Elsevier, 2022, pp. 319–341, https://doi.org/10.1016/B978-0-12-820558-7.00022-4.

[18] K. He, N. Chen, C. Wang, L. Wei, J. Chen, Method for determining crystal grain size by x-ray diffraction, Cryst. Res. Technol. vol. 53 (2) (2018) 1700157.

[19] S.M. Londoño-Restrepo, R. Jeronimo-Cruz, B.M. Millán-Malo, E.M. Rivera-Muñoz, M.E. Rodriguez-García, Effect of the nano crystal size on the x-ray diffraction patterns of biogenic hydroxyapatite from human, bovine, and porcine bones, Sci. Rep. vol. 9 (1) (2019) 5915, https://doi.org/10.1038/s41598-019-42269-9.

[20] A.V. Naumkin, A. Kraut-Vass, S.W. Gaarenstroom, C.J. Powell, NIST standard reference database 20, version 4.1, The National Institute of Standards and Technology NIST,, 2012, pp. 1–49.

[21] G. Hameed, A. Goksu, A. Merkouri, S.C. Ruiz, M.S. Duyar, Synthesis, testing and characterisation of silica-supported nickel phosphide reverse water-gas shift catalysts with varying Ni/P atomic ratios: supplementary materials. Mendeley Data, 2023. doi: 〈10.17632/ccxtpdyhfj.1〉.

[22] S.-K. Wu, P.-C. Lai, Y.-C. Lin, Atmospheric hydrodeoxygenation of guaiacol over nickel phosphide catalysts: effect of phosphorus composition, Catal. Lett. vol. 144 (5) (2014) 878–889, https://doi.org/10.1007/s10562-014-1231-7.

[23] X. Lan, R. Pestman, E.J.M. Hensen, T. Weber, Furfural hydrodeoxygenation (HDO) over silica-supported metal phosphides – the influence of metal–phosphorus

stoichiometry on catalytic properties, J. Catal. vol. 403 (2021) 181–193, https://doi.org/10.1016/j.jcat.2021.01.031.
[24] S.T. Oyama, X. Wang, Y.-K. Lee, K. Bando, F.G. Requejo, Effect of phosphorus content in nickel phosphide catalysts studied by XAFS and other techniques, J. Catal. vol. 210 (1) (2002) 207–217, https://doi.org/10.1006/jcat.2002.3681.
[25] W. Zhou, et al., The deoxygenation pathways of palmitic acid into hydrocarbons on silica-supported Ni12P5 and Ni2P catalysts, Catalysts vol. 8 (4) (2018), https://doi.org/10.3390/catal8040153.
[26] D. Lou, et al., A core-shell catalyst design boosts the performance of photothermal reverse water gas shift catalysis, Sci. China Mater. vol. 64 (2021) 2212–2220.
[27] Md.H. Al Rashid, X-ray absorption spectroscopy studies on the structure and the catalytic activity of nickel phosphide catalysts (Theses (doctoral)), Hokkaido University,, Sapporo, 2021.
[28] C. Hu, et al., General strategy for preparation of porous nickel phosphide nanosheets on arbitrary substrates toward efficient hydrogen generation, ACS Appl. Energy Mater. vol. 3 (1) (. 2020) 1036–1045, https://doi.org/10.1021/acsaem.9b02067.
[29] F. Wang, Y. Liu, C. Zhang, Facile synthesis of porous carbon/Ni 12 P 5 composites for electrocatalytic hydrogen evolution, N. J. Chem. vol. 43 (10) (2019) 4160–4167.
[30] D. Zeng, et al., Ni 12 P 5 nanoparticles embedded into porous gC 3 N 4 nanosheets as a noble-metal-free hetero-structure photocatalyst for efficient H 2 production under visible light, J. Mater. Chem. A Mater. vol. 5 (31) (2017) 16171–16178.
[31] M. Niu, et al., Well-defined ultrasmall V-NiP2 nanoparticles anchored g-C3N4 nanosheets as highly efficient visible-light-driven photocatalysts for h2 evolution, Catalysts vol. 12 (9) (2022), https://doi.org/10.3390/catal12090998.
[32] H. Tian, X. Wang, H. Li, M. Pi, D. Zhang, S. Chen, Superhydrophilic Al-Doped NiP2 nanosheets as efficient electrocatalysts for hydrogen evolution reaction, Energy Technol. vol. 8 (1) (2020) 1900936.
[33] X. Wang, H. Zhou, D. Zhang, M. Pi, J. Feng, S. Chen, Mn-doped NiP2 nanosheets as an efficient electrocatalyst for enhanced hydrogen evolution reaction at all pH values, J. Power Sources vol. 387 (2018) 1–8, https://doi.org/10.1016/j.jpowsour.2018.03.053.
[34] H. Shi, J. Chen, Y. Yang, S. Tian, Catalytic deoxygenation of methyl laurate as a model compound to hydrocarbons on nickel phosphide catalysts: Remarkable support effect, Fuel Process. Technol. vol. 118 (2014) 161–170, https://doi.org/10.1016/j.fuproc.2013.08.010.
[35] K. Li, R. Wang, J. Chen, Hydrodeoxygenation of anisole over silica-supported Ni2P, MoP, and NiMoP Catalysts, Energy Fuels vol. 25 (3) (. 2011) 854–863, https://doi.org/10.1021/ef101258j.
[36] Z. Pan, R. Wang, Z. Nie, J. Chen, Effect of a second metal (Co, Fe, Mo and W) on performance of Ni2P/SiO2 for hydrodeoxygenation of methyl laurate, J. Energy Chem. vol. 25 (3) (2016) 418–426, https://doi.org/10.1016/j.jechem.2016.02.007.
[37] O. Clause, L. Bonneviot, M. Che, Effect of the preparation method on the thermal stability of silica-supported nickel oxide as studied by EXAFS and TPR techniques, J. Catal. vol. 138 (1) (1992) 195–205, https://doi.org/10.1016/0021-9517(92)90017-C.
[38] P. Sirikulbodee, M. Phongaksorn, T. Sornchamni, T. Ratana, S. Tungkamani, Effect of different iron phases of Fe/SiO2 catalyst in CO_2 hydrogenation under mild conditions, Catalysts vol. 12 (7) (2022) 698.
[39] J.-Y. Jing, J.-Z. Wang, D.-C. Liu, Z.-Q. Qie, H.-C. Bai, W.-Y. Li, Naphthalene hydrogenation saturation over Ni2P/Al2O3 catalysts synthesized by thermal decomposition of hypophosphite, ACS Omega vol. 5 (48) (. 2020) 31423–31431, https://doi.org/10.1021/acsomega.0c05019.
[40] A.A. Munera Parra, C. Asmanoglo, D.W. Agar, Modelling and optimization of a moving-bed adsorptive reactor for the reverse water-gas shift reaction, Comput. Chem. Eng. vol. 109 (2018) 203–215, https://doi.org/10.1016/j.compchemeng.2017.11.013.
[41] U. Guharoy, T. Ramirez Reina, S. Gu, Q. Cai, Mechanistic insights into selective CO_2 conversion via RWGS on transition metal phosphides: a DFT study, J. Phys. Chem. C. vol. 123 (37) (. 2019) 22918–22931, https://doi.org/10.1021/acs.jpcc.9b04122.
[42] P. Riani, I. Valsamakis, T. Cavattoni, V. Sanchez Escribano, G. Busca, G. Garbarino, Ni/SiO2-Al2O3 catalysts for CO_2 methanation: Effect of La2O3 addition, Appl. Catal. B vol. 284 (2021), 119697, https://doi.org/10.1016/j.apcatb.2020.119697.
[43] R. Zhang, et al., Tuning reverse water gas shift and methanation reactions during CO_2 reduction on Ni catalysts via surface modification by MoOx, J. CO_2 Util. vol. 52 (2021), 101678, https://doi.org/10.1016/j.jcou.2021.101678.
[44] C.-S. Chen, C.S. Budi, H.-C. Wu, D. Saikia, H.-M. Kao, Size-tunable Ni nanoparticles supported on surface-modified, cage-type mesoporous silica as highly active catalysts for CO_2 hydrogenation, ACS Catal. vol. 7 (12) (. 2017) 8367–8381, https://doi.org/10.1021/acscatal.7b02310.
[45] Y. Liu, et al., Synergetic enhancement of activity and selectivity for reverse water gas shift reaction on Pt-Re/SiO2 catalysts, J. CO_2 Util. vol. 63 (2022), 102128, https://doi.org/10.1016/j.jcou.2022.102128.
[46] R. Mutschler, E. Moioli, W. Luo, N. Gallandat, A. Züttel, CO_2 hydrogenation reaction over pristine Fe, Co, Ni, Cu and Al2O3 supported Ru: Comparison and determination of the activation energies, J. Catal. vol. 366 (2018) 139–149, https://doi.org/10.1016/j.jcat.2018.08.002.
[47] Z. Ma, M.D. Porosoff, Development of tandem catalysts for CO_2 hydrogenation to olefins, ACS Catal. vol. 9 (3) (. 2019) 2639–2656, https://doi.org/10.1021/acscatal.8b05060.
[48] S. Ghosh, B. Mondal, S. Roy, M. Shalom, M.B. Sadan, Alcohol oxidation with high efficiency and selectivity by nickel phosphide phases, J. Mater. Chem. A Mater. vol. 10 (15) (2022) 8238–8244, https://doi.org/10.1039/D2TA00863G.
[49] Y. Chen, et al., Effect of nickel phosphide nanoparticles crystallization on hydrogen evolution reaction catalytic performance, Trans. Nonferrous Met. Soc. China vol. 27 (2) (2017) 369–376, https://doi.org/10.1016/S1003-6326(17)60041-4.
[50] J.A. Rodriguez, J.-Y. Kim, J.C. Hanson, S.J. Sawhill, M.E. Bussell, Physical and chemical properties of MoP, Ni2P, and MoNiP hydrodesulfurization catalysts: time-resolved X-ray diffraction, density functional, and hydrodesulfurization activity studies, J. Phys. Chem. B vol. 107 (26) (2003) 6276–6285, https://doi.org/10.1021/jp022639q.
[51] P. Liu, J.A. Rodriguez, Catalysts for hydrogen evolution from the [NiFe] hydrogenase to the Ni2P(001) surface: the importance of Ensemble Effect, J. Am. Chem. Soc. vol. 127 (42) (2005) 14871–14878, https://doi.org/10.1021/ja0540019.
[52] E. Muthuswamy, G.H.L. Savithra, S.L. Brock, Synthetic levers enabling independent control of phase, size, and morphology in nickel phosphide nanoparticles, ACS Nano vol. 5 (3) (2011) 2402–2411, https://doi.org/10.1021/nn1033357.
[53] E. le Saché, L. Pastor-Pérez, B.J. Haycock, J.J. Villora-Picó, A. Sepúlveda-Escribano, T.R. Reina, Switchable catalysts for chemical co2 recycling: a step forward in the methanation and reverse water–gas shift reactions, ACS Sustain Chem. Eng. vol. 8 (11) (2020) 4614–4622, https://doi.org/10.1021/acssuschemeng.0c00551.
[54] J. Gandara-Loe, Q. Zhang, J.J. Villora-Picó, A. Sepúlveda-Escribano, L. Pastor-Pérez, T. Ramirez Reina, Design of full-temperature-range RWGS catalysts: impact of alkali promoters on Ni/CeO2, Energy Fuels vol. 36 (12) (2022) 6362–6373, https://doi.org/10.1021/acs.energyfuels.2c00784.
[55] L.-P. Merkouri, E. le Saché, L. Pastor-Pérez, M.S. Duyar, T. Ramirez Reina, Versatile Ni-Ru catalysts for gas phase CO_2 conversion: bringing closer dry reforming, reverse water gas shift and methanation to enable end-products flexibility, Fuel vol. 315 (2022), 123097, https://doi.org/10.1016/j.fuel.2021.123097.
[56] Q. Sheng, X. Li, R. Prins, C. Liu, Q. Hao, S. Chen, Understanding the reduction of transition-metal phosphates to transition-metal phosphides by combining temperature-programmed reduction and infrared spectroscopy, Angew. Chem. Int. Ed. vol. 60 (20) (2021) 11180–11183.
[57] ThermoFisher Scientific. Accessed: 9 October 2023. [Online]. Available: ⟨https://www.thermofisher.com/uk/en/home/materials-science/learning-center/periodic-table.html⟩.
[58] M.C. Biesinger, X-ray Photoelectron Spectroscopy (XPS) reference pages. Surface Science Western, University of Western Ontario,, *Ontario*, 2015. Accessed: 9 October 2023. [Online]. Available, ⟨https://www.xpsfitting.com/search/label/Nickel⟩.
[59] L. Wan, J. Zhang, Y. Chen, C. Zhong, W. Hu, Y. Deng, Varied hydrogen evolution reaction properties of nickel phosphide nanoparticles with different compositions in acidic and alkaline conditions, J. Mater. Sci. vol. 52 (2) (2017) 804–814, https://doi.org/10.1007/s10853-016-0377-7.
[60] S. Carenco, Z. Liu, M. Salmeron, The birth of nickel phosphide catalysts: monitoring phosphorus insertion into nickel, ChemCatChem vol. 9 (12) (2017) 2318–2323.